Research Update: Emerging chalcostibite absorbers for thin-film solar cells

Francisco Willian de Souza Lucas[1,2] and Andriy Zakutayev[1,a]

[1]*Materials Science Center, National Renewable Energy Laboratory, Golden, Colorado 80401, USA*

[2]*Department of Chemistry, Federal University of Sao Carlos, São Carlos, SP 13565-905, Brazil*

Copper antimony chalcogenides $CuSbCh_2$ (Ch=S, Se) are an emerging family of absorbers studied for thin-film solar cells. These non-toxic and Earth-abundant materials show a layered low-dimensional chalcostibite crystal structure, leading to interesting optoelectronic properties for applications in photovoltaic (PV) devices. This research update describes the $CuSbCh_2$ crystallographic structures, synthesis methods, competing phases, band structures, optoelectronic properties, point defects, carrier dynamics, and interface band offsets, based on experimental and theoretical data. Correlations between these absorber properties and PV device performance are discussed, and opportunities for further increase in the efficiency of the chalcostibite PV devices are highlighted. © *2018 Author(s). All article content, except where otherwise noted, is licensed under a Creative Commons Attribution (CC BY) license (http://creativecommons.org/licenses/by/4.0/).* https://doi.org/10.1063/1.5027862

I. INTRODUCTION

The most studied materials for the thin-film photovoltaic (PV) technologies are $Cu(In,Ga)Se_2$ (CIGS, 22.6% one-sun energy conversion efficiency) and CdTe (22.1% efficiency).[1] Nevertheless, the future environmental benefits and potential scale of deployment of these solar cells may be limited by their elemental scarcity (In, Ga, Te) and toxicity (Cd).[2] These considerations have led to increased interest in emerging light-absorber materials with less toxic and more abundant elements, including Cu_2SnS_3 (CTS),[3] Cu_2O,[4] Sb_2Se_3,[5] Cu_3N,[6,7] SnS,[8,9] $ZnSnN_2$,[10] and $Cu_2ZnSn(S,Se)_4$ (CZTSSe).[11] Among these, the highest PV efficiency (certified 12.6%[1,12]) has been reported for the CZTSSe absorber. However, its further improvements may be hindered by chemical and crystallographic complexity, pointing researchers toward less complex materials.

Most of the emerging absorbers, like CZTSSe, have a three-dimensional (3D) crystal structure, where dangling bonds in grain boundaries (GBs) can act as recombination centers, causing efficiency loss.[13,14] In contrast, the low-dimensional crystal structure of some potential absorbers, such as 1D-Sb_2Se_3,[5,15] 1D-SbSeI,[16] 2D-$CuSbS_2$,[17] 2D-$CuBiS_2$,[18] and 2D-$CuSbSe_2$,[19] can be oriented hypothetically in such a way to decrease the number of dangling bonds, even at the GBs. In turn, this can minimize photoexcited charge-carrier recombination losses, which is one of the major limiting factors for high-efficiency thin-film solar cells.

One class of such non-toxic Earth-abundant less-complex and low-dimensional absorbers is ternary copper chalcogenides, such as $CuBiS_2$[18] and $CuSbCh_2$ (where Ch=S, Se) with a chalcostibite crystal structure.[17,19] Despite a relatively small amount of research, these layered semiconductors have shown promising PV device efficiencies approaching 5%.[19–21] The PV-relevant properties of these materials include slightly indirect bandgaps of 1.1–1.6 eV (that is, well-suited for single-junction terrestrial solar cell applications) and strong optical absorption coefficient >10^5 cm^{-1} at 0.5 eV above the bandgap (slightly better than CIGSe, CdTe, and CZTSSe, for example).[19,21–23]

---

[a]Author to whom correspondence should be addressed: andriy.zakutayev@nrel.gov

Many other characteristics that make these chalcostibite materials worth exploring will be discussed in this research update.

A good review of the PV applications of $CuSbS_2$ (CAS) was published three years ago,[24] but much $CuSbS_2$ research activity has occurred since that time, and there are no review papers about $CuSbSe_2$ (CASe) as a PV absorber. Thus, in this article, we focus on the most recent research efforts (past three years) on $CuSbCh_2$ (Ch=S, Se) as a promising family of absorber materials for thin-film solar cell applications. This paper summarizes both the currently used methods to prepare these materials and their most important PV-relevant properties, as compared to other thin-film PV absorbers. We also discuss the factors that have limited current $CuSbCh_2$-based solar cell performance, as well as some strategies that have been used to address them.

II. MATERIAL PROPERTIES

A. Crystallographic structure

As mentioned earlier, most of the absorbers used in solar cells have a tetrahedrally bonded lattice, where different atoms are linked to one another in 3D diamond-like structures (e.g., Si, CdTe, $CuInS_2$, and Cu_2ZnSnS_4), as can be seen in Fig. 1(a). However, the $CuSbCh_2$ chalcostibites show a very different 2D-like layered crystal structure, despite the same 1:1:2 stoichiometry as in $CuInS_2$ chalcopyrites, and similar Sb/In ionic radii.[25] In contrast to the four-fold coordinated chalcopyrite, in the chalcostibite structure the Cu atoms are four-fold coordinated, whereas the Sb atoms are in a distorted three-fold coordination [Fig. 1(b)]. This difference in the metal coordination number makes chalcostibites "line compounds": namely, the small deviations from the nominal $CuSbCh_2$ stoichiometry (Cu/Sb = 1) lead to phase impurities, indirectly suggesting a smaller propensity to cation disorder for the stoichiometric material. This is in contrast to the tetrahedrally coordinated CIGS, CTZS, and CTS, which are known to show cation disorder and to tolerate high levels of off-stoichiometry (up to ~20%).[25] The crystallographic differences between the 3D (e.g., $CuInS_2$), 2D (e.g., $CuSbS_2$), and 1D (e.g., Sb_2Se_3) absorbers can be seen in Fig. 1.

As can be seen in Fig. 1(b), the $CuSbCh_2$ crystal structure is formed by stacking layers composed of $SbSe_2$ and $CuSe_3$ motifs along the "c"-axis, with interlayer distances of ~7.10 Å (for Ch=S) and ~7.29 Å (for Ch=Se).[26] Theoretical calculations reveal that these layers (along with other characteristics) are responsible for the increase in the density of states (DOS) in $CuSbCh_2$ and that
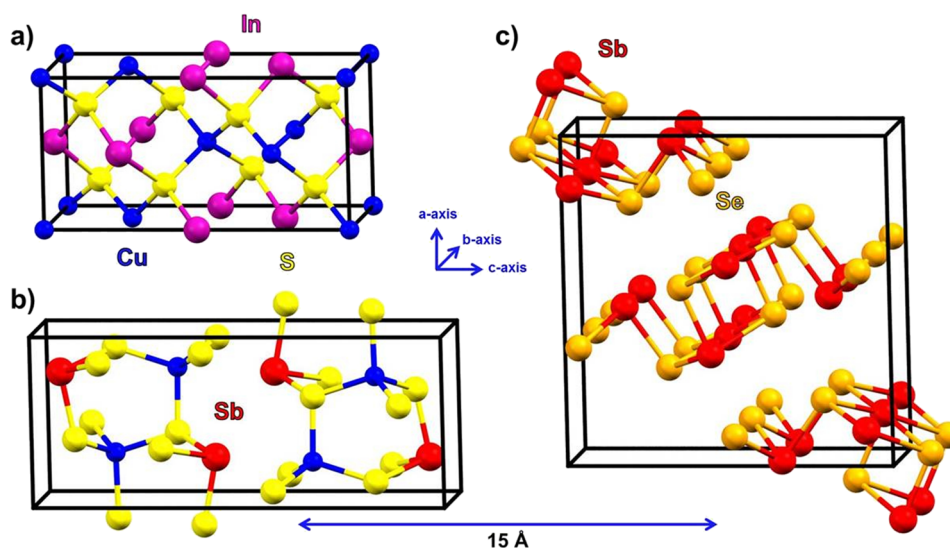

FIG. 1. Crystallographic structure of (a) $CuInS_2$, (b) $CuSbS_2$, and (c) Sb_2Se_3. The atoms are not at comparable scales with respect to each other, but the unit cells are, as defined by the 15-Å scale bar on the bottom of the figure. The crystal structure pictures were created using Mercury 3.9 (Copyright CCDC 2001-2016) and the CIF files from Inorganic Crystal Structure Database (Ref. 46).

each trivalent Sb atom has a non-bonding electron pair from its 5s orbital. These factors are responsible for the larger optical extinction coefficient of $CuSbCh_2$ than in CIGS, for example, but they also lead to higher effective masses and less efficient collection of the photogenerated charge carriers.[21,26–28]

Another interesting property that results from the low-dimensional structure is the possibility of crystallographically orienting the layers in different ways with respect to the substrate. Such preferential orientation may create chemically inert surfaces in 2D structures and benign grain boundaries (GBs) in 1D structures, both with fewer dangling bonds compared to the 3D structures. The benign surfaces or GBs can reduce the carrier recombination loss, improving the efficiency of thin-film solar cells. The preferential orientation is also important to the charge transport inside $CuSbCh_2$, which is easier within the sheets than between them. Within the $CuSbCh_2$ sheets, the carriers are transported along chemical bonds, whereas in the other case, they are required to hop between the layers, as in Sb_2Se_3.[19,21,22] Thus, the crystallographic orientation control is vital for reduced carrier recombination and improved carrier transport in $CuSbCh_2$ PV devices.[19,21,22]

B. Synthesis and secondary phases

A wide variety of techniques has been used to grow $CuSbCh_2$ and they can be grouped into physical and chemical methods. Physical methods include thermal evaporation[29] and co-sputtering,[19,30,31] whereas chemical methods include chemical bath deposition,[32,33] spray pyrolysis,[34] spin coating,[20,35] solution processing,[36] electrodeposition,[37,38] and solvo-/hydro-thermal synthesis.[39,40] Below, we focus mostly on the physical vapor deposition methods for $CuSbCh_2$ growth.

The control of the $CuSbCh_2$ composition during growth is very important because small deviations from the nominal stoichiometry more easily lead to phase impurities than in CIGS and CZTSSe.[25] For this reason, self-regulated growth (a.k.a. adsorption-controlled growth) is the most promising approach to achieve reproducible synthesis of this material, regardless of the deposition method. This kind of $CuSbCh_2$ growth control has been demonstrated for $CuSbCh_2$ by radio-frequency (RF) magnetron co-sputtering of Cu_2Ch and Sb_2Ch_3 targets in excess of Sb_2Ch_3 vapor.[19,21,22,41] For CAS, it was found that it is possible to grow highly stoichiometric phase-pure thin films at the substrate temperature of 350 °C in a wide range of Sb_2S_3 over-flux.[22] The CAS films showed some Sb_2S_3 impurities at lower temperatures or decomposed to $Cu_{12}Sb_4S_{13}$ at higher temperatures.

To determine the stability region for the deposition of stoichiometric phase-pure CAS films, the phase diagram has been calculated as a function of temperature and Sb_2S_3 partial pressure [Fig. 2(a)].[22] It was concluded that for a given substrate temperature, phase-pure $CuSbS_2$ can be grown in a ~10^2 Torr dynamic range of Sb_2S_3 partial pressure. In turn, for a given Sb_2S_3
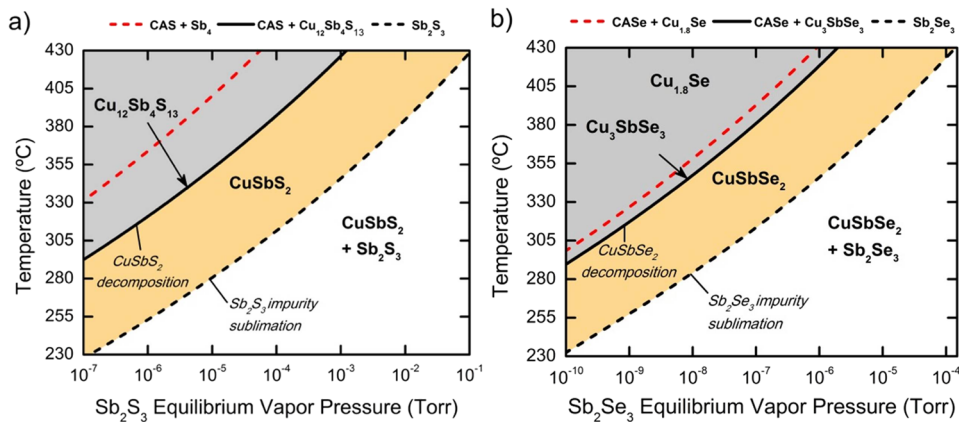

FIG. 2. Calculated phase diagrams for (a) Cu—Sb—S and (b) Cu—Sb—Se material systems, as a function of temperature and vapor pressure of Sb_2Ch_3, outlining the adsorption-limited self-regulated growth window for phase-pure $CuSbCh_2$ (orange region). Figures "(a)" and "(b)" were adapted from A. W. Welch *et al.*, Sol. Energy Mater. Sol. Cells **132**, 499 (2014). Copyright 2014 Elsevier B.V. and A. W. Welch *et al.*, Appl. Phys. Express **8**, 82301 (2015). Copyright 2015 The Japan Society of Applied Physics.

partial pressure, the region of stability extends ~70 °C of substrate temperature in agreement with experimental data. Overall, these results suggest that no fine control of the Sb_2S_3 precursor flux or substrate temperature is required within this region of $CuSbS_2$ self-regulated growth. Similar conclusions hold for $CuSbSe_2$ adsorption-controlled growth in an Sb_2Se_3-rich atmosphere, but at slightly higher temperatures (~380 °C), and with somewhat different competing phases [Sb_2Se_3, Cu_3SbSe_3, and Cu_2Se in Fig. 2(b)].

It is worth mentioning that the $CuSbCh_2$ films grown by different methods often show small grains and/or low crystallinity, encouraging the use of post-deposition thermal treatments (TTs) to improve film quality. Such a treatment has been demonstrated under atmospheric conditions,[30,35,42] H_2S gas and S vapor,[20] or Sb_2S_3 vapor.[30,31,43,44] For example, taking into account the calculated stability of the $CuSbCh_2$ phase under an Sb_2Ch_3-rich environment [Fig. 2(a)], it has been shown that the TT of the sputtered CAS thin films under Sb_2S_3 vapor increases their grain size without affecting the composition or phase purity. This TT also improved the structural quality and optoelectronic properties of the films, leading to more reproducible and efficient TT-$CuSbS_2$ PV devices.[44] In this context, it is also important to note that $CuSbCh_2$ has a lower melting point of 480 °C (for Ch=Se) and 535 °C (for Ch=S), compared to CIGS, CZTSSe, and CdTe (~1000 °C[21,45]). This should lead to grain growth at a lower temperature, making $CuSbCh_2$ a suitable absorber for the fabrication of flexible thin-film solar cells on polymer substrates.

Based on the experimental and calculated data shown in Fig. 2, the most likely impurities found in $CuSbCh_2$ (Ch=S or Se) are the following phases: Sb_2Ch_3, $Cu_{1.8-2}Ch$, $Cu_{12}Sb_4S_{13}$ (for the Cu-Sb-S system), and Cu_3SbSe_3 (for the Cu—Sb—Se system). As shown by the simulated X-ray diffraction (XRD) reference patterns in Fig. 3, there are several regions of superposition between the diffraction peaks of the $CuSbCh_2$ and impurity phases. For CAS [Fig. 3(a)], the most difficult impurity to identify by XRD is $Cu_{12}Sb_4S_{13}$ (12-4-13 phase) because its main peak is at the same position as the CAS (200)/(013) peaks. Thus, a common mistake made in the literature is attributing an increase in the (200)/(013) peaks compared to the (111)/(104) peaks to preferential orientation of CAS, instead of the actual presence of the very stable 12-4-13 secondary phase.

The Raman spectroscopy can be useful for determining the presence of this impurity because its main peak is ~20 cm^{-1} higher compared to the $CuSbS_2$ main peak at 332 cm^{-1}.[47] Also, the $CuSbS_2$ thin film with the $Cu_{12}Sb_4S_{13}$ phase impurity often has higher conductivity and higher hole density (10^{-1} to 10^2 S/cm and 10^{18}–10^{21} cm^{-3}) than phase-pure $CuSbS_2$ (10^{-3} to 10^{-2} S/cm and 10^{16}–10^{17} cm^{-3}). Thus, it should be possible to combine electric measurements with XRD and Raman spectroscopy characterizations to rule out the existence of the 12-4-13 phase.[22,41] The phase purity is equally important but less difficult to determine in $CuSbSe_2$ [Fig. 3(b)], where less stable Cu_3SbS_3
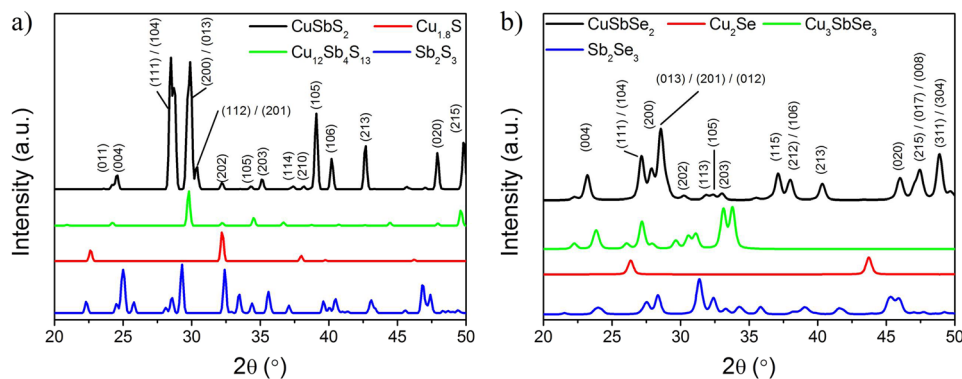

FIG. 3. Simulated X-ray diffraction reference patterns for the most likely impurities found in (a) $CuSbS_2$ and (b) $CuSbSe_2$ films after growth or thermal treatment. The following X-ray diffraction patterns were taken from Inorganic Crystal Structures Database (ICSD®)[46] and International Centre for Diffraction Data (ICDD®)–Powder Diffraction File (PDF™): $CuSbS_2$ (ICSD code 85133), $C_{1.8}S$ (ICSD code 69756), $Cu_{12}Sb_4S_{13}$ (ICSD code 25707), Sb_2S_3 (ICSD code 22176), $CuSbSe_2$ (ICDD-PDF card no. 75-992), $Cu_{1.8}Se$ (ICDD-PDF card no. 4-839), Cu_3SbSe_3 (ICDD-PDF card no. 50-1346), and Sb_2Se_3 (ICDD-PDF card no. 65-2433).

and $Cu_{1.8}Se$ secondary phases can be more easily identified by XRD, despite some overlap with the weaker $CuSbSe_2$ (113)/(105)/(203) peaks.

C. Band structure and optoelectronic properties

The knowledge of the band structure and DOS helps us to understand the optoelectronic properties of $CuSbCh_2$ compared with the more studied absorber materials such as CIS, as shown in Fig. 4. It has been predicted that chalcostibite $CuSbS_2$ and $CuSbSe_2$ have slightly indirect bandgaps [E_g^{dir}–E_g^{ind} ≈ 0.1 eV, Figs. 4(a) and 4(b)] in contrast with the well-defined direct bandgap of chalcopyrite $CuInSe_2$ [Fig. 4(c)]. Chalcostibites also present higher DOS compared to chalcopyrites. This band-structure feature not only results in a larger optical extinction coefficient (more effective absorption of photons) but also in higher effective masses (less efficient charge-carrier collection for the PV device).[28]

Theoretical calculations in combination with experimentally measured X-ray photoemission spectra show that the top of the valence band (VB) of CAS is mainly formed by strongly antibonding Cu 3d and S 3p states. In contrast, Sb 5p and S 3p states are main contributions for the bottom of the conduction band (CB).[28,48] It is also interesting to note that Sb 5s electrons in $CuSbCh_2$ are not fully inert and localized lone pairs. Instead, these Sb 5s states contribute somewhat to the formation of bonding states in the VB and antibonding states in the CB. These states are also partially associated with the rising of the energy levels of the bands,[48] which has important implications for the selection of contacts to $CuSbCh_2$ absorbers.

In agreement with the theoretical observations, the $CuSbCh_2$ materials feature strong experimental optical absorption coefficients of $>10^5$ cm^{-1} for photon energies 0.5 eV higher than their bandgaps,[19,21–23] as shown in Fig. 5(a), and have slightly indirect bandgaps of 1.1–1.2 eV[19,21] (for Ch=Se) and 1.4–1.6 eV (for Ch=S)[44] [Figs. 5(b) and 5(c)]. In Fig. 5(b), the presence of an electronic defect 0.22 eV below the bandgap energy can also be observed (i.e., 0.22 eV close to VB or CB); the different defects likely present in $CuSbCh_2$ samples will be discussed in Sec. II D.

$CuSbCh_2$ possesses p-type conductivity and presents a tunable hole concentration in a range of 10^{15}–10^{18} cm^{-3} suitable for PV application.[22] The hole mobility (μ_h) has been measured by the Hall effect, showing values of 0.1–49 cm^2 V^{-1} s^{-1} (for Ch=S)[35] and 12 cm^2 V^{-1} s^{-1} (for Ch=Se).[21] The large variation in the values of μ_h reported in the literature may be related to differences in both the concentration of defects and anisotropic crystal structures in combination with different crystallographic textures of the films. Based on optical-pump THz probe (OPTP) transient reflection spectroscopy, it has been observed that the hole and electron mobilities in 2D-like $CuSbS_2$ are similar to each other, in contrast to the significantly different hole and electron mobilities in 3D-bonded materials such as CIGS, CZTS, and CTS.[44]

D. Defects and carrier dynamics

Some of the most important characteristics of the PV absorbers that should be considered for their device performance are defect properties and photoexcited charge-carrier dynamics. Thus,
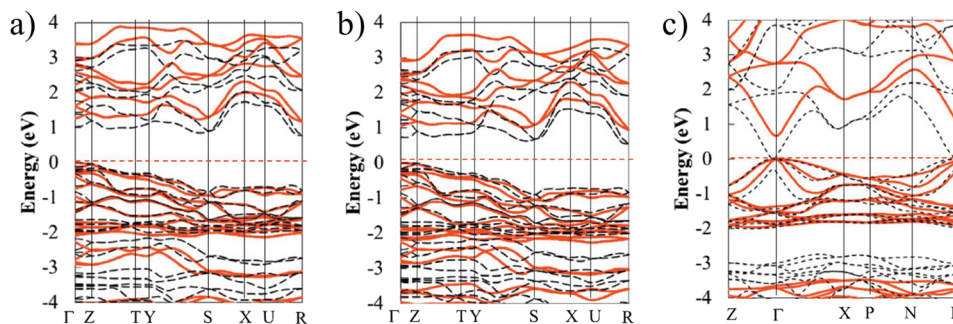

FIG. 4. Electronic band structure of chalcostibite-type (a) $CuSbS_2$ and (b) $CuSbSe_2$, in comparison with (c) the chalcopyrite-type $CuInSe_2$ band structure. The band structure calculated with HSE06 and GGA-PBE functionals are shown in solid (red) and dashed lines (black), respectively, and the valence band maximum (VBM) was set to 0 eV. Figures were adapted from T. Maeda and T. Wada, Thin Solid Films **582**, 401 (2015). Copyright 2015 Elsevier B.V.
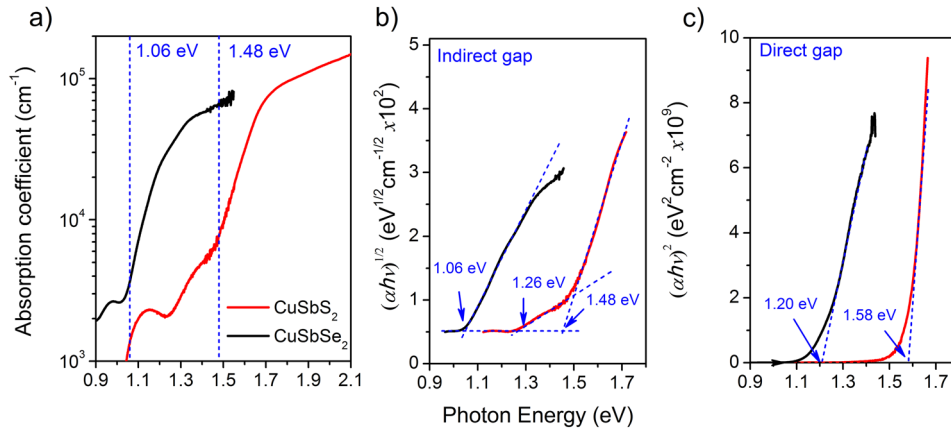
FIG. 5. Graphs of (a) optical absorption coefficient (α) *versus* photon energy ($h\nu$) and Tauc plots for the (b) indirect and (c) direct gaps for thin films of CuSbS$_2$ and CuSbSe$_2$. Data were adapted from A. W. Welch *et al.*, Sol. Energy Mater. Sol. Cells **132**, 499 (2014). Copyright 2014 Elsevier B.V. and A. W. Welch *et al.*, Appl. Phys. Express **8**, 82301 (2015). Copyright 2015 The Japan Society of Applied Physics.

despite a relatively small number of CuSbCh$_2$ publications on these topics, such studies are crucial for understanding CuSbCh$_2$ thin-film solar cell performance and for enhancing their efficiencies. There are many methods that can be used to study defects, including first-principles calculations, photoluminescence (PL) spectroscopy, admittance spectroscopy (AS), and deep-level transient spectroscopy (DLTS). The photoexcited charge-carrier dynamics can be studied using transient OPTP reflection spectroscopy and time-resolved photoluminescence (TRPL). Some of these techniques have been previously reported for studying defects and recombination in CuSbCh$_2$ materials.

First-principles calculations of native point defects in CuSbS$_2$[49] have been performed for different chemical potentials, such as the experimentally used Sb$_2$S$_3$-rich conditions [Fig. 6(a)]. The results show that the most plentiful acceptor is the copper vacancy (V$_{Cu}$), with a very shallow transition level (0/1−) at ~0.03 eV above the valence band maximum (VBM). Another active acceptor defect is the copper on antimony antisite (Cu$_{Sb}$), showing deeper transition levels of 0.1 and 0.2 eV. The likely dominant donor defects are Cu interstitials (within the layer—Cu$_{i\text{-in}}$ and between the layers—Cu$_{i\text{-out}}$), which are very shallow (transition levels close to the conduction band minimum, CBM). In addition, the sulfur vacancies (V$_{S\text{-in}}$ and V$_{S\text{-out}}$) also have relatively low formation enthalpy (ΔH_f). The (0/1+) transition level is around 0.15 eV and 0.35 eV for V$_{S\text{-out}}$ and V$_{S\text{-in}}$, respectively, and the (1+/2+) transition level for V$_{S\text{-out}}$ is around 0.10 eV. Hence, these vacancies are amphoteric defects that may
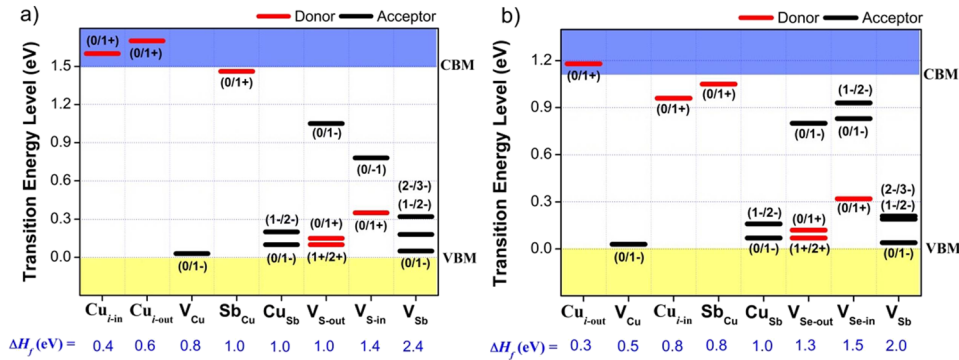

FIG. 6. Calculated transition energy levels, and formation enthalpy (ΔH_f), at simulated equilibrium Fermi level (E$_F$), for acceptor and donor intrinsic defects in (a) CuSbS$_2$ and (b) CuSbSe$_2$ at Sb$_2$Ch$_3$-rich condition. Data for figures (a) and (b) were adapted from F. W. de Souza Lucas *et al.*, J. Mater. Chem. A **5**, 21986 (2017). Copyright 2017 The Journal of Materials Chemistry A and A. W. Welch *et al.*, Adv. Energy Mater. **7**, 1601935 (2017). Copyright 2017 WILEY-VCH Verlag GmbH & Co. KGaA, Weinheim, respectively.
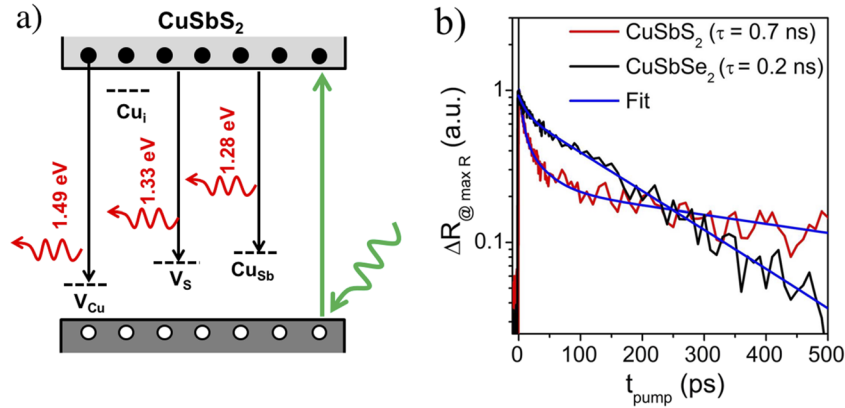
FIG. 7. (a) Simplistic diagram for experimental photoluminescent transitions observed in CuSbS$_2$ thin films. Figure adapted from F. W. de Souza Lucas *et al.*, J. Mater. Chem. A **5**, 21986 (2017). Copyright 2017 The Journal of Materials Chemistry A. (b) Time-domain optical pump-terahertz probe (OPTP) differential reflectance for CuSbCh$_2$ thin films, showing the tri-exponential fit to determine the carrier lifetime (τ). Data for this figure were adapted from F. W. de Souza Lucas *et al.*, J. Phys. Chem. C **120**, 18377 (2016). Copyright 2016 American Chemical Society and A. W. Welch *et al.*, Adv. Energy Mater. **7**, 1601935 (2017). Copyright 2017 WILEY-VCH Verlag GmbH & Co. KGaA, Weinheim.

act as donors or as acceptors, depending on the position of the Fermi level (E$_F$). These data are in agreement with the previously reported properties of defects in CuSbS$_2$.[35] Similar conclusions for CuSbSe$_2$[19,26] can be made, as can be seen in Fig. 6(b).

From an experimental point of view, defects in different CuSbS$_2$ samples (as-deposited, TT, and micro-crystals) have been studied by AS, PL, and DLTS.[49] Three acceptor defects were found at about 0.08, 0.17, and 0.24 eV above the VBM by the capacitance-based methods, in agreement with free-to-bound radiative photoluminescent transitions observed in these thin films. Comparing these results to the theoretical calculation [Fig. 6(a)], the shallower defect was associated with V$_{Cu}$, whereas the two deeper ones were attributed to Cu$_{Sb}$ and/or V$_S$, as can be seen in the diagram of Fig. 7(a). No investigation of the experimental behavior of the CuSbSe$_2$ defects can be found in the literature.

To understand the effects of point defects on CuSbCh$_2$ photoexcited charge carriers, transient OPTP reflection spectroscopy [a.k.a time-resolved terahertz spectroscopy (TRTS)] has been performed. An experimental study of the carrier dynamics in the solution-processed CuSbS$_2$ nanoplates[33] indicates a minority lifetime (τ) of up to ~1 ns and a mobility (μ) of ~1 cm^2 V^{-1} s^{-1}, which result in a diffusion length (L$_d$) estimate of ~60 nm [L$_d$ = (kTμτ/e)$^{1/2}$ Ref. 21]. Similar results have been

TABLE I. Summary of optoelectronic properties of CuSbCh$_2$ (CAS and CASe), Cu$_2$ZnSn(S,Se)$_4$ (CZTSSe), and Cu(In,Ga)Se$_2$ (CIGS). p = Hole concentration, and μ_h = majority-carrier mobility measured by the Hall effect. m^* = "e" or "h" effective masses, m_0 = electron rest mass (9.1 × 10^{-31} kg). τ = minority-carrier lifetime measured by [#]transient optical-pump THz probe (OPTP) reflection spectroscopy or [$]time-resolved photoluminescence (TRPL). α = absorption coefficient for photon energy 0.5 eV higher than the bandgap energy (E_g).

Material	p (cm^{-3})	m^* (m_0)	μ_h (cm^2 V^{-1} s^{-1})	τ (ns)	α (cm^{-1})	E_g (eV)
CAS	10^{16}–10^{20} (Ref. 41)	m^*_e = 2.9 m^*_h = 3.7 (Ref. 41)	0.1–49 (Ref. 35)	[#]0.5–1.3 (Ref. 33)	> 10^5 (Ref. 44)	1.4–1.6 (Ref. 44)
CASe	10^{16}–10^{18} (Ref. 21)	m^*_e = 2.5 (Ref. 21)	12 (Ref. 21)	[#]0.2–1.3 (Ref. 21)	> 10^5 (Refs. 19 and 21)	1.1–1.2 (Refs. 19 and 21)
CZTSSe	10^{15}–10^{16} (Ref. 50)	m^*_e = 0.07–0.18 m^*_h = 0.2–2 (Ref. 51)	6 (Ref. 50)	[$]1–10 (Ref. 50)	> 10^4 (Ref. 51)	1.0–1.6 (Ref. 51)
CIGS	10^{14}–10^{17} (Ref. 52)	m^*_e = 0.26 (Ref. 53)	1–100 (Ref. 53)	[$]64 (Ref. 54)	> 10^4 (Ref. 52)	1.0–1.6 (Ref. 52)

shown using the OPTP for the thermally treated $CuSbS_2$ films (τ of 0.7 ns, μ of ~4 cm^2 V^{-1} s^{-1}, and estimated L_d of ~90 nm).[44] The photoexcited charge-carrier dynamics in $CuSbSe_2$ thin films studied using the OPTP indicate higher μ (~12 cm^2 V^{-1} s^{-1}), but smaller τ (0.2 ns), and hence similar L_d (~80 nm). Figure 7 shows the time-domain OPTP spectra for $CuSbS_2$ and $CuSbSe_2$ thin films.

Finally, a summary of the important optoelectronic properties of the chalcostibite $CuSbCh_2$ is shown in Table I, in comparison with the chalcopyrite $Cu(In,Ga)Se_2$ and kesterite $Cu_2ZnSn(S,Se)_4$. Overall, both chalcostibites show similar properties to one another but somewhat different if compared to chalcopyrites and kesterites. Despite the higher absorption coefficient shown by the 2D chalcostibite materials, they show larger effective masses of charge carriers and lower photoexcited charge-carrier lifetime. However, the carrier concentrations and the bandgaps of chalcostibites and chalcopyrites/kesterites are quite similar.

III. DEVICE PERFORMANCE

A. Band offsets and contacts

Advancing from intrinsic properties of the $CuSbCh_2$ material to $CuSbCh_2$ device integration, the development of suitable front contacts (also known as "buffers") and back contacts is an important direction of research. This is related to the anisotropic properties of the layered $CuSbCh_2$ structure, which makes the surface energies, densities of surface states, and energy band positions [ionization potentials (IP) and electron affinities (χ)] different than in CIGS and related absorbers. First-principles calculations indicate that $CuSbS_2$ has two lower-energy surfaces: the (001)-plane with a surface energy of 12.4 meV Å^{-1} [(a) and (b) planes in Fig. 1(c)] and the (010)-plane with 14.6 meV Å^{-1}. As shown in Fig. 8(a), the (001) surface has a lower density of surface states than the (010) surface, which is consistent with the weak bonding of the (001) planes. Figure 8(b) shows the calculated energy band positions for [001]- and [010]-oriented $CuSbS_2$ absorber surfaces compared to the commonly used CdS contact layer. These results suggest a cliff-type $CuSbS_2$/CdS band offset of 0.85–1.43 eV, depending on the surface orientation.[41]

Experimental measurements of IP and work function (Φ) on CAS thin films have been performed by X-ray photoemission spectroscopy (XPS)[48] and ultraviolet photoemission spectroscopy (UPS).[35] XPS for the as-deposited and thermally treated $CuSbS_2$ is shown in Fig. 9(a). The IP of 4.98/5.25 eV (XPS/UPS) and the Φ of 4.73/4.86 eV (XPS/UPS) were found. Combining these results with the experimentally measured direct/indirect bandgap energy (1.58 eV/1.48 eV[41]) of the $CuSbS_2$ and the estimated band position of the CdS buffer (IP of 7.1 eV $vs.$ vacuum level and bandgap of 2.6 eV[55]), the CBM of this absorber is expected to be 0.7–1.1 eV higher than that of CdS. These experimental results (Fig. 9) are consistent with the theoretical results (Fig. 8) and suggest the presence of interfacial recombination centers.[56] Temperature-dependent J–V measurements (JV–T) performed on $CuSbS_2$/CdS devices [Fig. 9(b)] showed an open-circuit voltage (V_{OC}) extrapolated to 0 K of ~0.7 V,
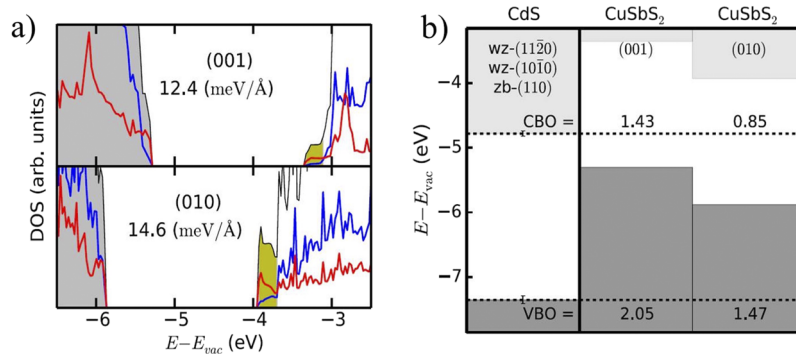

FIG. 8. First-principles calculated (a) density of states (DOS) of $CuSbS_2$ surface slabs, normalized by the surface area and offset such that the Fermi level is at zero, and (b) expected band offsets for the lowest-energy [00l]- and [010]-$CuSbS_2$ surfaces with various CdS surfaces. The yellow areas in (a) are the surface states, whereas the red and blue lines are projections onto the surface and bulk, respectively. These figures were adapted from A. W. Welch $et\ al.$, Prog. Photovoltaics Res. Appl. **24**, 929 (2015). Copyright 2015 John Wiley & Sons, Ltd.
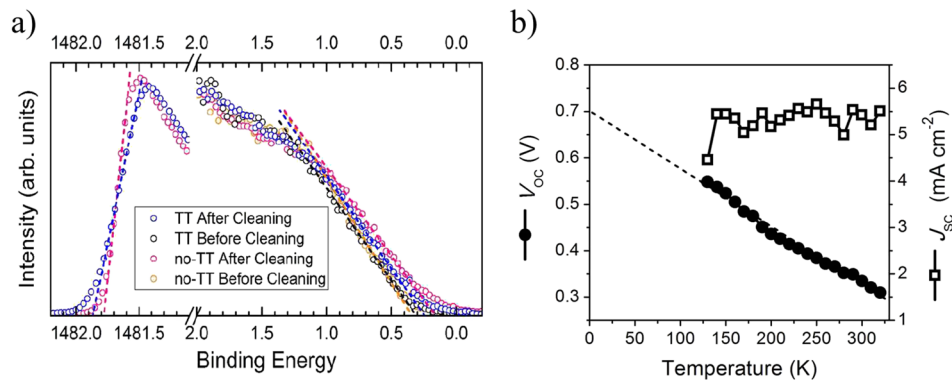
FIG. 9. (a) Fittings of the valence band maximum (VBM) and secondary electron cutoff (SEC) from XPS spectra for the as-deposited and thermally treated $CuSbS_2$ films, before and after surface cleaning. The Fermi level is at 0 eV. (b) Short-circuit current density (J_{SC}) and open-circuit voltage (V_{OC}) data from temperature-dependent J-V measurements on a $CuSbS_2$/CdS device. Figures (a) and (b) were adapted from T. J. Whittles *et al.*, ACS Appl. Mater. Interfaces **9**, 41916 (2017). Copyright 2017 American Chemical Society and F.W. de Souza Lucas *et al.*, J. Mater. Chem. A 5, 21986 (2017). Copyright 2017 American Michaelis Society, respectively.

also indicative of a 0.7–0.9 eV cliff-type band offset at the $CuSbS_2$/CdS interface.[44] In contrast, the Fermi level and VBM of $CuSbSe_2$ measured by UPS are −4.63 eV and −4.88 eV with respect to vacuum level (0 eV), respectively.[26] Thus, $CuSbSe_2$ may have a less detrimental CB offset with CdS, compared to $CuSbS_2$.

Motivated by the high CB offset between the $CuSbCh_2$ absorber and the commonly used CdS contact, some research has been directed at alternative buffer layers, such as undoped and Ga-doped $Cd_{1-x}Zn_xS$ deposited by atomic layer deposition.[57] The $CuSbS_2$ devices made with Zn-rich undoped buffers ($Cd_{0.61}Zn_{0.39}S$ and $Cd_{0.14}Zn_{0.86}S$) showed high series resistance and very low photoresponse, but 2.4%–5.5% Ga doping in $Cd_{0.6}Zn_{0.4}S$ partially addressed these problems. Comparing the performance of the standard chemical-bath-deposited CdS, V_{OC} improved from 211 mV to 449 mV, the short-circuit current density (J_{SC}) improved from 3.82 to 6.24 mA cm^{-2}, and the efficiency increased from ∼0.3% to 1%. Addressing the issue of Cd toxicity, the CdS/ZnO layers were replaced with GaN/$In_{0.15}Ga_{0.85}N$ in CAS devices, achieving the efficiency of ∼3% and the highest value of J_{SC} (∼34 mA cm^{-2}) reported in the literature,[31] which is above the theoretical limit for this 1.5 eV bandgap material.

Different back-contact materials have been also evaluated for CAS PV devices, such as Au, W, Ni, Pd, Pt, FTO, and Mo.[41] Many of these back contacts did not result in functioning PV devices due to delamination, pinholes, interface reaction, or other reasons. Among these back contacts, Mo provided the best current collection, even though its work function (4.35–4.90 eV[58]) was not favorable for charge extraction from the $CuSbS_2$ absorber. Thus, for improving the back contact, the effect of the addition of charge-selective layers (CSLs) on Mo was also studied.[41] The MoO_x CSL-based device showed a significant increase in efficiency (from 0.49% to 0.86%) because of the improvement in J_{SC} (from 3.53 to 8.91 mA cm^{-2}). This effect on J_{SC} was explained by the deeper (6.6 eV[59]) work function of the MoO_x layer, which promotes an upward band bending in the absorber, reflecting the photogenerated electrons.[41] A similar device with a sulfurized hybrid ink/spin-coated $CuSbS_2$ thin-film absorber has shown a record efficiency of 3.22% and J_{SC} of 15 mA cm^{-2} (see Table II), albeit without statistical histograms or certification results reported in the paper.[20] This high performance may be related to the carbon-containing layer at the Mo/$CuSbS_2$ interface measured by Auger electron spectroscopy (AES) depth profiling, which may also aid charge selection.

B. Photovoltaic devices

For the most part, $CuSbCh_2$ research has so far focused on the intrinsic optoelectronic properties of the materials (e.g., absorption coefficient, bandgap, carrier concentration). However, significant

TABLE II. Summary of $CuSbS_2$(CAS) and $CuSbSe_2$(CASe) photovoltaic devices with different architectures and for different methods of absorber growth.

No	Device architecture	V_{OC} (mV)	J_{SC} (mA cm^{-2})	FF	Efficiency (%)
1	Mo/C-rich CAS/$^{£,\$b}$CAS/CdS/ZnO/ZnO:Al/Al[20]	470	15.64	0.44	3.22[a]
2	Mo/$^{\#}$CAS/CdS/ZnO/ZnO:Al/Al[41]	330	3.53	0.41	0.49
3	Mo/MoO$_X$/$^{\#}$CAS/CdS/ZnO/ZnO:Al/Al[41]	309	8.91	0.31	0.86
4	Mo/$^{\#,\$c}$CAS/CdS/ZnO/ZnO:Al/Al[44]	350	5.20	0.55	1.0
5	FTO/$^{£,\$a}$CAS/CdS/ZnO/ZnO:Al/Au[35]	440	3.65	0.31	0.5
6	$hv{\rightarrow}$FTO/CdS/i-Sb$_2$S$_3$/$^{\not c,\$a}$CAS/C/Ag[24]	405	7.54	0.32	1.0
7	Mo/$^{@,\$b}$CAS/CdS/ZnO:Al[20]	490	14.73	0.44	3.13[b]
8	Mo/$^{\#,\$a}$CAS/CdS/GaN/ITO[30]	104	1.29	0.26	0.04
9	Mo/$^{\#,\$c}$CAS/CdS/In$_{0.3}Ga_{0.7}$ N/ITO[30]	251	8.58	0.31	0.76
10	Mo/TiN/$^{\#,\$c}$CAS/GaN/In$_{0.15}Ga_{0.85}$ N/ITO[31]	295	33.78[c]	0.30	2.99
11	Mo/$^{£,\$a}$CA(S$_{0.08}$,Se$_{1.92}$)/CdS/ZnO/ZnO:Al/Au[42]	360	20.52	0.37	2.70
12	Mo/$^{\#}$CASe/CdS/ZnO/ZnO:Al/Ni-Al[21]	336	26.0	0.53	4.70
13	Mo/Na-doped $^{\#}$CASe/CdS/ZnO/ZnO:Al/Ni-Al[21]	394	19.0	0.57	4.28
14	Mo/$^{\#}$CASe/CdS/ZnO/ZnO:Al/Ni-Al[21]	346	20.5	0.44	3.5
15	FTO/$^{£,\$a}$CASe/CdS/ZnO/ITO/Al[26]	274	11.84	0.40	1.32

[a]Efficiency without statistical histograms.

[b]Details of the device characterization are still lacking.

[c]Value above the theoretical limit for this 1.5 eV bandgap material. The absorbers were fabricated by (#) co-sputtering, (£) solution-processed/spin-coating, or (@) electrodeposition of metallic stack. $. The absorbers were thermally treated under (a) low vacuum, (b) H$_2$S$_{(g)}$/S$_{(vapor)}$, or (c) Sb$_2$Se$_{3(vapor)}$ atmosphere. $\not c$. CBD of Sb$_2$S$_3$ and thermal evaporation of Cu. The "$hv{\rightarrow}$" symbol indicated the direction of incident light in the superstrate configuration.

challenges arise on integrating absorber thin films into PV device prototypes,[19] such as the choice of adequate back/front contacts, growth of pinhole-free absorber layers, optimization of absorber thickness, and possible chemical reactions or inter-diffusion of the absorber with contacts. All of these parameters are very time-consuming to evaluate using the traditional experimental approach. To address this challenge, high-throughput experimental (HTE) combinatorial research methods[60,61] can be extended from materials studies[62,63] to accelerate PV device research.[64,65]

The first attempt to apply the HTE approach to $CuSbCh_2$ devices has focused on studying the effects of the crystallographic orientation, phase purity, composition, morphology, and thickness of the $CuSbS_2$ absorber on the PV performance of devices with the SiO_2/Mo/$CuSbS_2$/CdS/i-ZnO/Al-ZnO/Al architecture and on evaluating different back contacts.[41] In this particular research, a <1%-efficient device was obtained with the optimal absorber thickness of 0.8 μm and MoO$_X$ CSL (device #3 in Table II).[41] Further, an improvement in $CuSbS_2$ PV device performance (1%) and reproducibility was achieved after absorber thermochemical treatment (TT) under Sb$_2$S$_3$ vapor followed by selective KOH chemical etch of a likely Sb$_2$S$_3$ surface layer, prior to the deposition of front contacts (device #4 in Table II).[44]

A similar HTE approach was also applied in the accelerated development of 3%–5%-efficient $CuSbSe_2$ devices (device #12 in Table II) and to understand the tradeoffs of light absorption and charge transport in these layered materials.[19,21] In an effort to suppress the tradeoff between J_{SC} and V_{OC} observed in this drift PV device, the Na incorporation in the absorber was investigated. The Na incorporation has enhanced V_{OC} by ~50 mV (comparing device #13 with #12 in Table II), but it also caused a decrease in J_{SC} and efficiency.[21] Several other adjustments in the device fabrication process were attempted, compared to the baseline device (#14 in Table II).[19] Some improvement of the efficiency resulted from using an MgF anti-reflection coating and from better design of the front-contact collector grids.[21]

Comparing the performances of the $CuSbS_2$ and $CuSbSe_2$ devices with similar structure (e.g., devices #4 and #12 in Fig. 10 and Table II), it is seen that V_{OC} for both materials is 300–400 mV [Fig. 10(a)], which is very low compared to their bandgaps (1.1–1.5 eV). This effect may be directly related to the low quasi Fermi-level splitting due to insufficient absorber quality, and to large CB offset at the interface between these absorbers and the commonly used CdS front contacts. However, the $CuSbSe_2$ devices have shown higher efficiencies, mainly caused by higher J_{SC} values. The
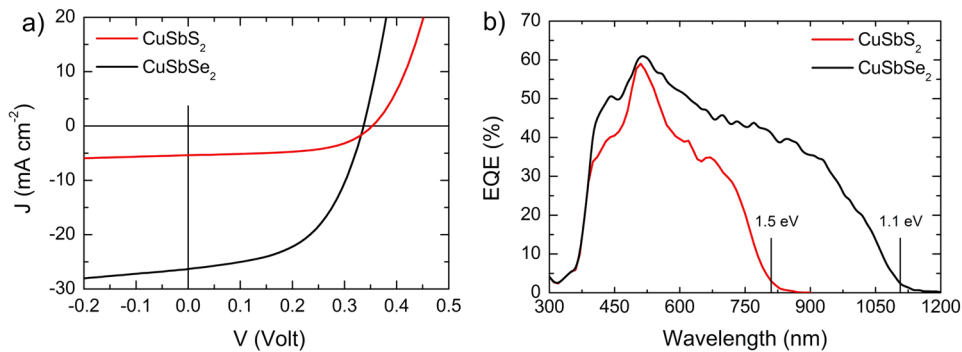
FIG. 10. (a) J–V curves under simulated AM1.5G illumination (100 mW cm^2) at 25 °C and (b) external quantum efficiency (EQE) for the CuSbCh$_2$ PV device. Data for figures (a) and (b) were adapted from F. W. de Souza Lucas *et al.*, J. Mater. Chem. A **5**, 21986 (2017). Copyright 2017 American Chemical Society (CuSbS$_2$) and A. W. Welch *et al.*, Adv. Energy Mater. **7**, 1601935 (2017). Copyright 2017 WILEY-VCH Verlag GmbH & Co. KGaA, Weinheim (CuSbSe$_2$).

higher J$_{SC}$ may be related to the better overlap of the CuSbSe$_2$ absorption with the solar spectrum indicated by better external quantum efficiency (EQE) [Fig. 10(b)] and by lower recombination of the photogenerated charge carriers at the front interface. To represent this comparison, Fig. 10 shows comparative graphs of current density-voltage (J-V) and EQE for these CuSbCh$_2$ PV devices. The poor carrier collection for photon energies near the band edge can be observed in both CuSbS$_2$ and CuSbSe$_2$ EQE graphs [Fig. 10(b)], which is mainly indicative of the short transport lengths of the photogenerated charge carriers.

In addition to the traditional substrate architecture (CIGS-like) of the PV devices described earlier, several other devices in substrate architectures and one in superstrate architectures (CdTe-like) have been attempted. These diverse CuSbCh$_2$ PV device configurations and performances are summarized in Table II. Most of the CuSbCh$_2$ PV device prototypes fabricated in the substrate configuration have the glass/back-contact/CuSbCh$_2$/buffer/TCO/front-contact architecture, where TCO is a transparent conductive oxide such as Al:ZnO or Sn:In$_2$O$_3$. Only one of the PV devices has a superstrate configuration with the glass/TCO/CuSbCh$_2$/buffer/back-contact architecture (i.e., device #6 in Table II), where TCO is F:SnO$_2$. So far, substrate devices had higher efficiencies than this superstrate device, further supporting the analogy of CuSbCh$_2$ materials with CIGS. However, in both cases, more research and development toward higher-quality absorbers and suitable contacts is needed to improve the efficiencies of CuSbCh$_2$ PV devices.

IV. SUMMARY

This article provides a research update on the emerging chalcostibite family of absorber materials for thin-film photovoltaic solar cells, with particular focus on the most recent research efforts (past 3 years). The CuSbCh$_2$ (Ch═S, Se) features layered the 2D-like chalcostibite crystallographic structure, in contrast to the 3D-like chalcopyrite structure of CuInSe$_2$ and CuGaSe$_2$. Because of the narrow composition phase width of CuSbCh$_2$, these absorber materials require a self-regulated adsorption-limited synthesis method to avoid detrimental Cu-rich competing phases such as Cu$_{12}$Sb$_4$S$_3$ or Cu$_2$Se. The band structure and optoelectronic properties of CuSbCh$_2$ feature higher density of states and optical absorption, but heavier effective masses and worse charge transport, compared to CIGS. The moderate hole density is set by compensation between copper vacancies and interstitials, whereas the charge recombination and carrier dynamics are determined by chalcogen vacancies and Cu-on-Sb antisites. The PV-relevant optoelectronic properties of CuSbS$_2$ and CuSbSe$_2$ are summarized in Table I, where they are also compared with the more studied CIGS and CZTS absorbers.

Both CuSbS$_2$ and CuSbSe$_2$ have large cliff-like interface band offsets with CdS, calling for further development of the chalcostibite contacts. The chalcostibite photovoltaic device efficiencies are currently limited to 1%–3% for CuSbS$_2$ and 3%–5% for CuSbSe$_2$ by short transport lengths of the photogenerated charge carriers and by detrimental voltage and current effects of the contact band offset. Hence, more research is needed on the chalcostibite absorber quality and contact selection.

Table II summarizes device architectures and the resulting device performances of different $CuSbCh_2$ solar cells reported in the literature. In summary, chalcostibite $CuSbCh_2$ materials are a promising non-toxic and Earth-abundant family of absorbers for applications in thin-film photovoltaic solar cell devices.

ACKNOWLEDGMENTS

[1] See https://www.nrel.gov/pv/assets/images/efficiency-chart.png for Best research-cell efficiencies (last accessed January 2018).

[2] C. Wadia, A. P. Alivisatos, and D. M. Kammen, Environ. Sci. Technol. **43**, 2072 (2009).

[3] M. Yang, A. Zakutayev, J. Vidal, X. Zhang, D. S. Ginley, and F. J. DiSalvo, Energy Environ. Sci. **6**, 2994 (2013).

[4] T. Minami, Y. Nishi, and T. Miyata, Appl. Phys. Express **8**, 22301 (2015).

[5] Y. Zhou, L. Wang, S. Chen, S. Qin, X. Liu, J. Chen, D. J. Xue, M. Luo, Y. Cao, Y. Cheng, E. H. Sargent, and J. Tang, Nat. Photonics **9**, 409 (2015).

[6] C. M. Caskey, R. M. Richards, D. S. Ginley, and A. Zakutayev, Mater. Horiz. **1**, 424 (2014).

[7] A. Zakutayev, C. M. Caskey, A. N. Fioretti, D. S. Ginley, J. Vidal, V. Stevanovic, E. Tea, and S. Lany, J. Phys. Chem. Lett. **5**, 1117 (2014).

[8] V. Steinmann, R. Jaramillo, K. Hartman, R. Chakraborty, R. E. Brandt, J. R. Poindexter, Y. S. Lee, L. Sun, A. Polizzotti, H. H. Park, R. G. Gordon, and T. Buonassisi, Adv. Mater. **26**, 7488 (2014).

[9] A. Sánchez-Juárez, A. Tiburcio-Silver, and A. Ortiz, Thin Solid Films **480-481**, 452 (2005).

[10] L. Lahourcade, N. C. Coronel, K. T. Delaney, S. K. Shukla, N. A. Spaldin, and H. A. Atwater, Adv. Mater. **25**, 2562 (2013).

[11] T. Gershon, B. Shin, N. Bojarczuk, M. Hopstaken, D. B. Mitzi, and S. Guha, Adv. Energy Mater. **5**, 1400849 (2015).

[12] K. Ramasamy, M. A. Malik, and P. O'Brien, Chem. Sci. **2**, 1170 (2011).

[13] R. Baier, C. Leenndertz, D. Abou-Ras, M. C. Lux-Steiner, and S. Sadewasser, Sol. Energy Mater. Sol. Cells **130**, 124 (2014).

[14] M. S. Leite, M. Abashin, H. J. Lezec, A. Gianfrancesco, A. A. Talin, and N. B. Zhitenev, ACS Nano **8**, 11883 (2014).

[15] M. B. Costa, F. W. de Souza Lucas, and L. H. Mascaro, ChemElectroChem **4**, 2507 (2017).

[16] C. Tablero, J. Alloys Compd. **678**, 18 (2016).

[17] A. Zakutayev, L. L. Baranowski, A. W. Welch, C. A. Wolden, and E. S. Toberer, in *2014 IEEE 40th Photovoltaic Specialist Conference (PVSC)* (IEEE, 2014), pp. 2436–2438.

[18] A. Gassoumi, M. Musa Saad H.-E., S. Alfaify, T. Ben Nasr, and N. Bouarissa, J. Alloys Compd. **725**, 181 (2017).

[19] A. W. Welch, L. L. Baranowski, P. Zawadzki, S. Lany, C. A. Wolden, and A. Zakutayev, Appl. Phys. Express **8**, 82301 (2015).

[20] S. Banu, S. J. Ahn, S. K. Ahn, K. Yoon, and A. Cho, Sol. Energy Mater. Sol. Cells **151**, 14 (2016).

[21] A. W. Welch, L. L. Baranowski, H. Peng, H. Hempel, R. Eichberger, T. Unold, S. Lany, C. Wolden, and A. Zakutayev, Adv. Energy Mater. **7**, 1601935 (2017).

[22] A. W. Welch, P. P. Zawadzki, S. Lany, C. A. Wolden, and A. Zakutayev, Sol. Energy Mater. Sol. Cells **132**, 499 (2014).

[23] L. Shi, Y. Li, C. Wu, and Y. Dai, J. Alloys Compd. **648**, 507 (2015).

[24] B. Krishnan, S. Shaji, and R. Ernesto Ornelas, J. Mater. Sci.: Mater. Electron. **26**, 4770 (2015).

[25] L. L. Baranowski, P. Zawadzki, S. Lany, E. S. Toberer, and A. Zakutayev, Semicond. Sci. Technol. **31**, 123004 (2016).

[26] D. J. Xue, B. Yang, Z. K. Yuan, G. Wang, X. Liu, Y. Zhou, L. Hu, D. Pan, S. Chen, and J. Tang, Adv. Energy Mater. **5**, 1501203 (2015).

[27] L. Yu, R. S. Kokenyesi, D. A. Keszler, and A. Zunger, Adv. Energy Mater. **3**, 43 (2013).

[28] T. Maeda and T. Wada, Thin Solid Films **582**, 401 (2015).

[29] A. Rabhi, M. Kanzari, and B. Rezig, Thin Solid Films **517**, 2477 (2009).

[30] W. L. Chen, D. H. Kuo, and T. T. A. Tuan, J. Electron. Mater. **45**, 688 (2015).

[31] A. D. Saragih, D. H. Kuo, and T. T. A. Tuan, J. Mater. Sci.: Mater. Electron. **28**, 2996 (2017).

[32] C. Macías, S. Lugo, Á. Benítez, I. López, B. Kharissov, A. Vázquez, and Y. Peña, Mater. Res. Bull. **87**, 161 (2017).

[33] M. E. Edley, B. Opasanont, J. T. Conley, H. Tran, S. Y. Smolin, S. Li, A. D. Dillon, A. T. Fafarman, and J. B. Baxter, Thin Solid Films **646**, 180 (2018).

[34] J. A. Ramos Aquino, D. L. Rodriguez Vela, S. Shaji, D. A. Avellaneda, and B. Krishnan, Phys. Status Solidi C **13**, 24 (2016).

[35] B. Yang, L. Wang, J. Han, Y. Zhou, H. Song, S. Chen, J. Zhong, L. Lv, D. Niu, and J. Tang, Chem. Mater. **26**, 3135 (2014).

[36] S. Suehiro, K. Horita, M. Yuasa, T. Tanaka, K. Fujita, Y. Ishiwata, K. Shimanoe, and T. Kida, Inorg. Chem. **54**, 7840 (2015).

[37] L. Zhang, Y. Li, X. Li, C. Li, R. Zhang, J. J. Delaunay, and H. Zhu, Nano Energy **28**, 135 (2016).

[38] D. Tang, J. Yang, F. Liu, Y. Lai, J. Li, and Y. Liu, Electrochim. Acta **76**, 480 (2012).

[39] H. Su, Solid State Ionics **123**, 319 (1999).

[40] C. An, Q. Liu, K. Tang, Q. Yang, X. Chen, J. Liu, and Y. Qian, J. Cryst. Growth **256**, 128 (2003).

[41] A. W. Welch, L. L. Baranowski, P. Zawadzki, C. DeHart, S. Johnston, S. Lany, C. A. Wolden, and A. Zakutayev, Prog. Photovoltaics Res. Appl. **24**, 929 (2016).

[42] B. Yang, C. Wang, Z. Yuan, S. Chen, Y. He, H. Song, R. Ding, Y. Zhao, and J. Tang, Sol. Energy Mater. Sol. Cells **168**, 112 (2017).

[43] F. W. De Souza Lucas, A. W. Welch, L. L. Baranowski, P. C. Dippo, L. H. Mascaro, and A. Zakutayev, in *2015 IEEE 42nd Photovoltaic Specialist Conference (PVSC)* (IEEE, 2015), pp. 1–5.

[44] F. W. de Souza Lucas, A. W. Welch, L. L. Baranowski, P. C. Dippo, H. Hempel, T. Unold, R. Eichberger, B. Blank, U. Rau, L. H. Mascaro, and A. Zakutayev, J. Phys. Chem. C **120**, 18377 (2016).

[45] X. Song, X. Ji, M. Li, W. Lin, X. Luo, and H. Zhang, Int. J. Photoenergy **2014**, 1.

[46] See http://www.fiz-karlsruhe.de/icsd.html for Inorganic Crystal Structure Database (last accessed January 2018).

[47] T. Rath, A. J. MacLachlan, M. D. Brown, and S. A. Haque, J. Mater. Chem. A **3**, 24155 (2015).

[48] T. J. Whittles, T. D. Veal, C. N. Savory, A. W. Welch, F. W. De Souza Lucas, J. T. Gibbon, M. Birkett, R. J. Potter, D. O. Scanlon, A. Zakutayev, and V. R. Dhanak, ACS Appl. Mater. Interfaces **9**, 41916 (2017).

[49] F. W. de Souza Lucas, H. Peng, S. Johnston, P. C. Dippo, S. Lany, L. H. Mascaro, and A. Zakutayev, J. Mater. Chem. A **5**, 21986 (2017).

[50] T. Gokmen, O. Gunawan, and D. B. Mitzi, Appl. Phys. Lett. **105**, 33903 (2014).

[51] U. Saha and M. K. Alam, RSC Adv. **7**, 4806 (2017).

[52] U. Rau, "Electronic properties of Cu(In,Ga)Se$_2$ thin-film solar cells: An update," in *Advances in Solid State Physics*, edited by B. Kramer (Springer, Berlin, Heidelberg, 2004), Vol. 44.

[53] See www.materials.nrel.gov for Effective masses and other electronic structure parameters (last accessed December 2017).

[54] J. V. Li, S. Grover, M. A. Contreras, K. Ramanathan, D. Kuciauskas, and R. Noufi, Sol. Energy Mater. Sol. Cells **124**, 143 (2014).

[55] S. M. Park, T. G. Kim, Y. D. Chung, D.-H. Cho, J. Kim, K. J. Kim, Y. Yi, and J. W. Kim, J. Phys. D: Appl. Phys. **47**, 345302 (2014).

[56] T. Minemoto, T. Matsui, H. Takakura, Y. Hamakawa, T. Negami, Y. Hashimoto, T. Uenoyama, and M. Kitagawa, Sol. Energy Mater. Sol. Cells **67**, 83 (2001).

[57] L. L. Baranowski, S. Christensen, A. W. Welch, S. Lany, M. Young, E. S. Toberer, and A. Zakutayev, Mater. Chem. Front. **1**, 1342 (2017).

[58] D. L. Jacobson and A. E. Campbell, Metall. Mater. Trans. B **2**, 3063 (1971).

[59] C. Battaglia, X. Yin, M. Zheng, I. D. Sharp, T. Chen, S. McDonnell, A. Azcatl, C. Carraro, B. Ma, R. Maboudian, R. M. Wallace, and A. Javey, Nano Lett. **14**, 967 (2014).

[60] M. L. Green, I. Takeuchi, and J. R. Hattrick-Simpers, J. Appl. Phys. **113**, 231101 (2013).

[61] M. L. Green, C. L. Choi, J. R. Hattrick-Simpers, A. M. Joshi, I. Takeuchi, S. C. Barron, E. Campo, T. Chiang, S. Empedocles, J. M. Gregoire, A. G. Kusne, J. Martin, A. Mehta, K. Persson, Z. Trautt, J. Van Duren, and A. Zakutayev, Appl. Phys. Rev. **4**, 11105 (2017).

[62] L. L. Baranowski, P. Zawadzki, S. Christensen, D. Nordlund, S. Lany, A. C. Tamboli, L. Gedvilas, D. S. Ginley, W. Tumas, E. S. Toberer, A. Zakutayev, S. David, W. Tumas, E. S. Toberer, and A. Zakutayev, Chem. Mater. **26**, 4951 (2014).

[63] P. P. Rajbhandari, A. Bikowski, J. D. Perkins, T. P. Dhakal, and A. Zakutayev, Sol. Energy Mater. Sol. Cells **159**, 219 (2017).

[64] S. Siol, T. P. Dhakal, G. S. Gudavalli, P. P. Rajbhandari, C. Dehart, L. L. Baranowski, and A. Zakutayev, ACS Appl. Mater. Interfaces **8**, 14004 (2016).

[65] K. Mokurala, L. L. Baranowski, F. W. De Souza Lucas, S. Siol, M. F. A. M. Van Hest, S. Mallick, P. Bhargava, and A. Zakutayev, ACS Comb. Sci. **18**, 583 (2016).